HRTEM Study of Oxide Nanoparticles in Fe-16Cr ODS Ferritic Steel Developed for Fusion Energy

L. L. Hsiung

June 25, 2010

Microscopy: Science, Technology, Applications and Education

Disclaimer

This document was prepared as an account of work sponsored by an agency of the United States government. Neither the United States government nor Lawrence Livermore National Security, LLC, nor any of their employees makes any warranty, expressed or implied, or assumes any legal liability or responsibility for the accuracy, completeness, or usefulness of any information, apparatus, product, or process disclosed, or represents that its use would not infringe privately owned rights. Reference herein to any specific commercial product, process, or service by trade name, trademark, manufacturer, or otherwise does not necessarily constitute or imply its endorsement, recommendation, or favoring by the United States government or Lawrence Livermore National Security, LLC. The views and opinions of authors expressed herein do not necessarily state or reflect those of the United States government or Lawrence Livermore National Security, LLC, and shall not be used for advertising or product endorsement purposes.

HRTEM Study of Oxide Nanoparticles in Fe-16Cr ODS Ferritic Steel Developed for Fusion Energy

Luke L. Hsiung

Lawrence Livermore National Laboratory
Physical and Life Sciences Directorate
L-352, P.O. Box 808
Livermore, CA, U.S.A.

1. ABSTRACT

Crystal and interfacial structures of oxide nanoparticles in Fe-16Cr ODS ferritic steel fabricated by mechanical alloying (MA), hot extrusion, and heat treatment have been examined using high-resolution transmission electron microscopy (HRTEM) techniques. A partial crystallization of oxide nanoparticles was frequently observed in as-fabricated ODS steel. The crystal structure of crystalline oxide particles is identified to be mainly $Y_4Al_2O_9$ (YAM) with a monoclinic structure. Orientation relationship between the oxide and the matrix are dependent on the particle size. Large nanoparticles with a diameter larger than 20 nm tend to be incoherent and have a nearly spherical shape, whereas small nanoparticles with a diameter smaller than 10 nm tend to be coherent or semi-coherent and have faceted interfaces with the matrix. The oxide nanoparticles become fully crystallized after prolonged annealing at 900 °C. These results lead us to propose a three-stage formation mechanism of oxide nanoparticles in ODS steels.

2. INTRODUCTION

Development of high-performance structural materials for first wall and breeding-blanket structural components, which will be exposed to high fluxes of high energy neutrons (14 MeV) and helium or alpha particles (3.6 MeV) from deuterium-tritium fusion, is one of the major challenges in materializing future fusion reactors. The choice of structural materials for the first wall and blanket components to a large degree dictates the design of the reactor systems. The selection of suitable structural materials is based on conventional properties (such as thermophysical, mechanical, and corrosion and compatibility), low neutron-induced radioactivity, and resistance to radiation-induced damage phenomena like material hardening/embrittlement and/or dimensional instability caused by void- and helium-driven swelling [1]. Oxide dispersion strengthened (ODS) ferritic/martensitic and ferritic steels, which produced by mechanical alloying the elemental (or pre-alloyed) metallic powder and yttria (Y_2O_3) oxide powder consolidated by hot extrusion or hot isostatic pressing, are advanced structural materials with a potential to be used at elevated temperatures due to the dispersion of thermally stable oxide nanoparticles into the matrix. The use of ODS steels should improve creep strength and oxidation/corrosion resistance at high temperatures and consequently increase the operating temperature of first wall and blanket structures in the future fusion reactors by approximately 700 °C or higher [2]. The performance of ODS steels is largely determined by the particle size and the stability of dispersed oxide nanoparticles. Although Y_2O_3 has been selected as the major dispersed oxide, its particle size increases during the consolidation and thermomechanical treatment of ODS steels. To enhance the stability of oxide particles, titanium and aluminum are added to form complex oxide with Y_2O_3 so as to make the dispersed oxides finer and more stable [2, 3]. Complex mechanisms involving fragmentation, dissolution/decomposition of Y_2O_3 particles, and reprecipitation of complex-oxide nanoparticles were previously proposed by Okuda and Fujiwara [4], Kimura et al. [5], Sakasegawa et al. [6], and Alinger et al. [7] based on the results generated from x-ray diffraction, TEM, atom probe tomography (APT), and small angle neutron scattering (SANS) studies. However, recent investigations conducted by Marquis [8] using APT and Klimiankou et al. [9] using EDX and EELS methods have discovered the existence of complex-oxide core associated with solute-enriched shell structures in oxide nanoparticles, which reveal that the previously proposed dissolution/reprecipitation mechanisms might not be the whole story. HRTEM study of nanoparticles in K3-ODS was thus conducted to examine the crystal and interfacial structures of oxide nanoparticles in order to better understand the formation mechanism of oxide nanoparticles in ODS steels.

3. EXPERIMENTAL

The material used for this investigation was 16Cr-4Al-2W-0.3Ti-0.3Y_2O_3 (K3) ODS ferritic steel [10]. Details of the fabrication process of the ODS steels can be found elsewhere [11]. Briefly, the pre-alloyed powder was first mechanically alloyed with Y_2O_3 powder in an Argon gas atmosphere at room temperature using an attrition type ball mill. The powder was then sealed in a stainless-steel can and degassed at 400 °C in 0.1 Pa pressure. The canned powders were subsequently consolidated by a hot extrusion technique at 1150 °C. After the extrusion, the consolidated K3-ODS steel was thermally treated at 1050 °C for 1 hour. One ODS steel sample was also annealed at 900 °C, 168 hours (one week) for a thermal stability study. The chemical composition (in wt.%) of the consolidated material is C: 0.08, Si: 0.033, Cr: 16, W: 1.82, Al: 4.59, Ti: 0.28, Y_2O_3: 0.368, and Fe: balance [10]. Thin foils for TEM analysis were prepared by a standard procedure that includes slicing, grinding, and polishing the recovered fragments with the foils surface approximately perpendicular to the loading axis. Final thinning of the foils was performed using a standard twin-jet electropolishing technique in an electrolyte (90 vol.% acetic acid, 10 vol.% perchloric acid) at 30 V and room temperature. Microstructural characterization was performed using Phillips CM300 field-emission transmission electron microscope (accelerating voltage of 300 kV). A software package CaRIne Crystallography 3.1 was used to simulate electron diffraction patterns in order to identify the crystal structures of ODS nanoparticles.

4. RESULTS AND DISCUSSION

Typical microstructures of K3-ODS steel are shown in Figs. 1a and 1b. Elongated grains (Fig. 1a) and dense oxide nanoparticles (Fig. 1b), mainly $Y_4Al_2O_9$ (YAM) complex oxide, were observed. The oxide nanoparticle sizes in K3-ODS (Fig. 1b) are mostly ranging between 1.7 nm and 30 nm, with a mean particle size of 5.91 nm, and a particle density of 1.33 x 10^{22} m^{-3}. Here an orientation relationship between $Y_4Al_2O_9$ oxide phase and the matrix can be derived from the selected-area diffraction pattern: $(0\bar{1}1)_\alpha \parallel (2\bar{4}2)_{YAM}$ and $[011]_\alpha \parallel [432]_{YAM}$. The formation of $Y_4Al_2O_9$ oxide particles was identified and confirmed by matching several observed and simulated diffraction patterns of different zone axes, and an example is shown in Fig. 2 for the $[432]_{YAM}$-zone pattern. $Y_4Al_2O_9$ has a monoclinic structure and space group: $P2_1/c$ with a = 0.7375 nm, b = 1.0507 nm, c = 1.1113 nm, and β = 108.58° [12, 13], which is illustrated in Fig. 2c. By comparing the $Y_4Al_2O_9$ nanoparticles formed in the ODS steel with the starting Y_2O_3 particles (space group: Ia_3, a cubic structure with a_o = 1.06 nm [13], particle size: 15-30 nm [14]) used to fabricate the ODS steel, one can realize that the formation of oxide nanoparticles in ODS steels does not take place solely through a fragmentation mechanism. The formation of $Y_4Al_2O_9$ complex oxide requires the decomposition of Y_2O_3: $Y_2O_3 \rightarrow 2[Y] + 3[O]$ and the internal oxidation reactions: $2[Al] + 3[O] \rightarrow Al_2O_3$ and $2Y_2O_3 + Al_2O_3 \rightarrow Y_4Al_2O_9$ during MA and consolidation, in which the internal oxidation reactions are governed by the oxygen affinity of alloying elements. That is, the formation of Y-Al complex oxides becomes predominant when both Al and Ti are present in ODS steels, which is in agreement with a conclusion made by Kasada et al [3].
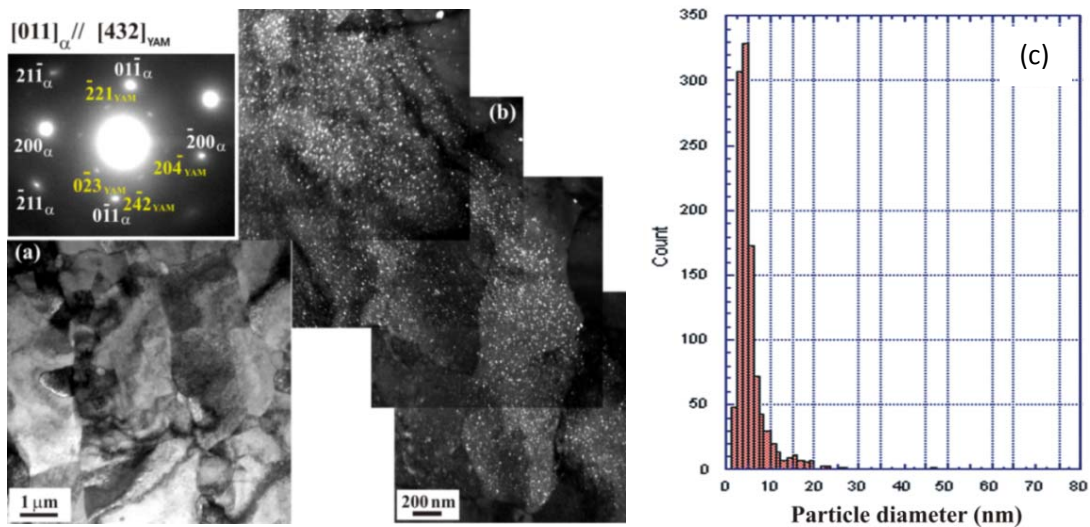
Fig. 1. (a) Bright-field TEM image shows typical grain morphology of K3-ODS steel, (b) dark-field TEM image and selected-area diffraction pattern of the $[011]_{Fe-Cr(\alpha)} \parallel [432]_{YAM}$-zone show the formation of dense $Y_4Al_2O_9$ nanoparticles in K3-ODS steel. (c) Size distribution of oxide nanoparticles measured from micrographs obtained using energy-filtered microscopy.
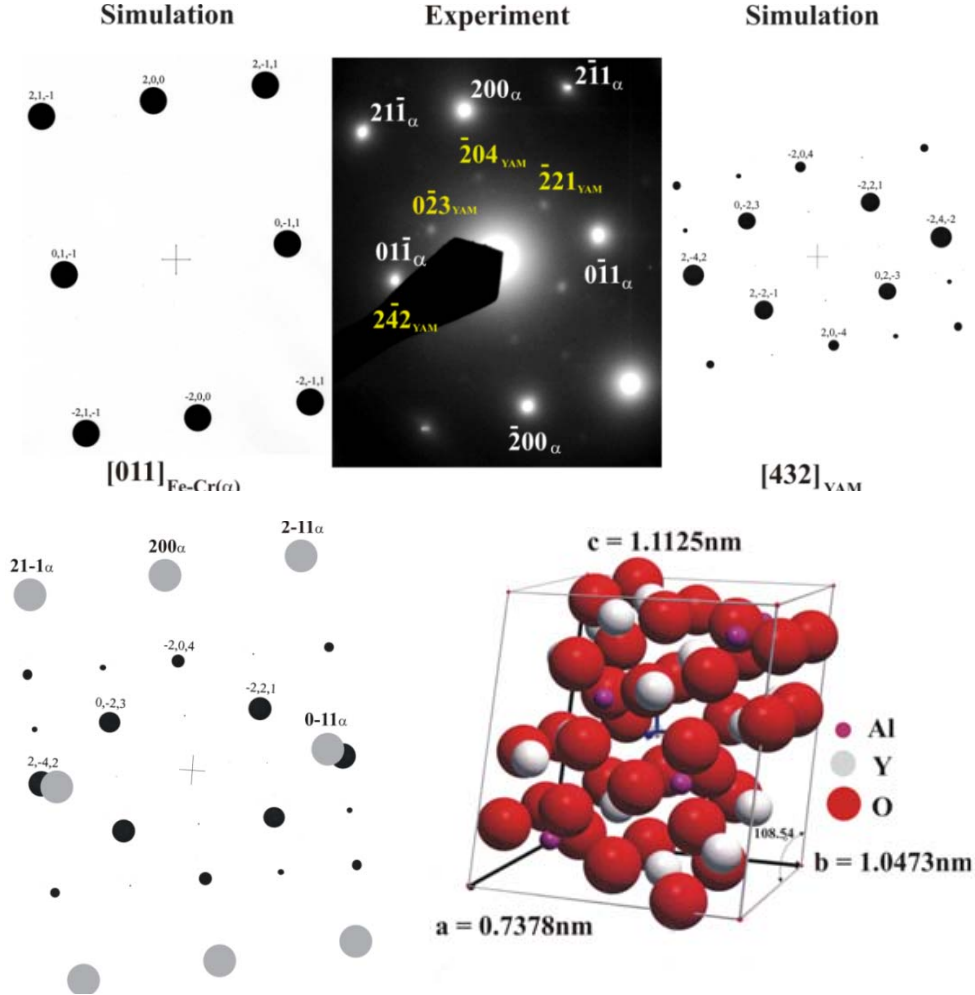

Fig. 2. (a) Observed and simulated diffraction patterns of the $[011]_{Fe-Cr(\alpha)}$-zone and the $[432]_{YAM}$-zone for identifying the formation of $Y_4Al_2O_9$ complex-oxide nanoparticles; (b) the overlap of simulated $[011]_{Fe-Cr(\alpha)}$-zone and $[432]_{YAM}$-zone diffraction patterns; (c) the crystal structure of $Y_4Al_2O_9$ complex-oxide compound .

Since the majority of oxide nanoparticles observed in K3-ODS steel has a diameter ranging between 2 nm and 30 nm, more attention was paid to nanoparticles smaller than 30 nm. HRTEM images of a large (> 20 nm) and a small (< 10 nm) $Y_4Al_2O_9$ nanoparticles in K3-ODS steel sample are shown in Figs. 3 and 4, respectively. The large nanoparticle (viewing from the $[100]_{YAM}$ direction) tends to be nearly spherical in shape and is incoherent with the matrix. In addition, one can distinguish the core region with an appearance of lattice fringes from the outer shell region with a featureless appearance. The images of the large nanoparticle taken from two different defocus conditions seem to indicate that the lower portion of the large nanoparticle contains a disordered (or amorphous) domain that appears no clear lattice fringes as those appeared on the upper portion of the nanoparticle. In other words, the large nanoparticle is in fact not fully crystallized. On the other hand, ledges and facets can be seen at the interface between the small nanoparticle and the matrix, as shown in Figs. 4a and 4b, which indicates that the small nanoparticle tends to be coherent or semi-coherent with the matrix. In addition, small featureless domains can be readily found at the oxide/matrix interface shown in Fig. 4a. Here an orientation relationship between the $Y_4Al_2O_9$

oxide and the matrix, which is different from that in Figs. 1, can be derived from the fast Fourier transformation (FFT) image shown in Fig. 4: $(0\bar{1}1)_\alpha \parallel (\bar{1}\bar{1}5)_{YAM}$ and $[011]_\alpha \parallel [732]_{YAM}$. Figure 5 may shed some light on why featureless domains at the oxide/matrix interfaces form. Here nucleation of a crystalline $Y_4Al_2O_9$ domain (2 x 5 nm in size) can be clearly seen within a partially crystallized nanoparticle. The orientation relationship between the crystalline $Y_4Al_2O_9$ domain and the matrix, which can be derived from the FFT image: $(0\bar{1}1)_\alpha \parallel (2\bar{4}2)_{YAM}$ and $[011]_\alpha \parallel [432]_{YAM}$, is the same as that in Figs. 1. Figure 6 shows another feature that can only be explained by the crystallization of amorphous oxide particle. Here two crystalline $Y_4Al_2O_9$ domains, designated as the $[432]_I$ domain and the $[221]_{II}$ domain, were identified within a nanoparticle. The interfacial structure and orientation relationship between the $[432]_I$ domain and the matrix are the same to the oxide/matrix interface shown in Fig. 5. The interfacial structure and orientation relationship between the $[221]_{II}$ domain and the matrix are shown in Fig. 7. Additional orientation relationship is found between the oxide nanoparticle and matrix: $(0\bar{1}1)_\alpha \parallel (2\bar{3}2)_{YAM}$ and $[011]_\alpha \parallel [221]_{YAM}$. In general, facets, ledges, interface dislocations, and small amorphous domains are common features observed from the interfaces shown in Figs. 4a, 5b, and 6b. The two orientation relationships between the oxide nanoparticle and the matrix reveal that the {011} planes of the matrix act as habit planes for the nucleation of $Y_4Al_2O_9$ nanoparticles; the faceted and ledged oxide/matrix interfaces indicate the growth of small nanoparticles through a ledge mechanism.

Figure 6 shows the result of an ODS steel sample annealed at 900 °C for 168 hours. Here a small nanoparticle (< 10 nm) remains faceted, and a large nanoparticle (> 20 nm) becomes perfectly spherical and fully crystallized without a core/shell structure. The observation of oxide nanoparticle without a core/shell structure after prolonged annealing seems to suggest that the core/shell structures of oxide nanoparticles formed in the as-fabricated ODS steels are far from chemical equilibrium. A revised three-stage formation mechanism of oxide nanoparticles is accordingly proposed based on the above HRTEM observations: (1) Fragmentation of starting Y_2O_3 particles to form finely-dispersed (nano or sub-nano) fragments during the early stages of ball milling; (2) Agglomeration and amorphization of fragments mixed with matrix material to form clusters and agglomerates (designated as [MYO], M = Fe, Cr, Al, W, Ti) during the later stages of ball milling; (3) Crystallization of the amorphous oxide agglomerates to form oxide nanoparticles with a stoichiometric complex-oxide core and a solute-enriched (M′) shell during consolidation. The contents of complex-oxide core and solute-enriched shell are dependent on the compositions of different ODS steels. Y-Al complex-oxide ($Y_xAl_yO_z$) cores can form in Al-contained ODS steels such as the currently studied 16Cr-ODS, Y-Ti complex-oxide ($Y_xTi_yO_z$) cores can form in Ti-contained ODS steels with no addition of Al such as MA957 steel [8], and Y_2O_3 cores can form in ODS steels with no additions of Al and Ti such as Eurofer 9Cr-ODS steel [9]. The solute-enriched shells can be perceived as a result of the depletion of the solutes that are not involved in the internal oxidation reactions for the complex-oxide cores such as Cr-enriched shells in the nanoparticles of MA957 and Mn- and V-enriched shells in the nanoparticles of Eurofer 9Cr-ODS steel [8, 9]. The shell thickness is dependent on the size of nanoparticles since the larger the particle the more matrix material will participate in the agglomeration and amorphization stage and thus more solutes will be depleted from the oxide core during the crystallization stage. A solute-enriched shell forms when solute depletion rate from the core is greater than solute diffusion rate from the oxide/matrix interface during the crystallization stage.

5. Summary

The oxide nanoparticles formed in 16Cr-4Al-2W-0.3Ti-0.3Y_2O_3 (K3) ODS steel are mainly $Y_4Al_2O_9$ (YAM) with a monoclinic structure. Large nanoparticles (> 20 nm) have a spherical shape and tend to be incoherent with the matrix; small nanoparticles (< 10 nm) accompany with facets and ledges at the oxide/matrix interfaces and tend to be coherent or semi-coherent with the matrix. Three different orientation relationships between small nanoparticles and the matrix were reported. A structure of crystalline oxide core in association with amorphous shell was observed in both large and small nanoparticles in as-fabricated K3-ODS steel. The core/shell structure vanishes after prolonged annealing at 900 °C for 168 hours, which suggests that the core/shell structure of oxide nanoparticles are far from chemical equilibrium. A three-stage formation mechanism of ODS nanoparticles including fragmentation, amorphization, and crystallization is accordingly proposed to rationalize the core/shell structures of nanoparticles observed in as-fabricated ODS steels.
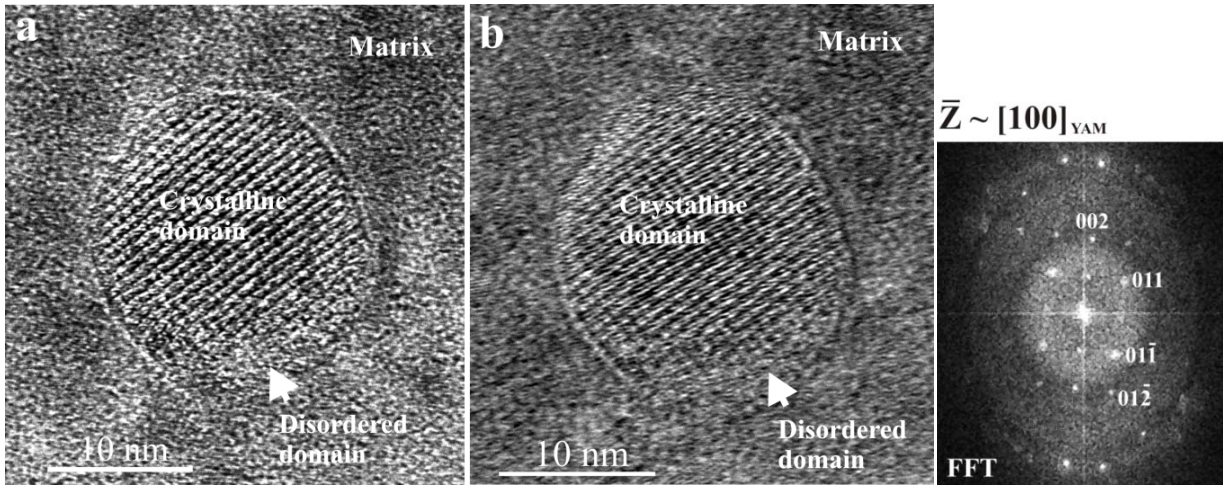
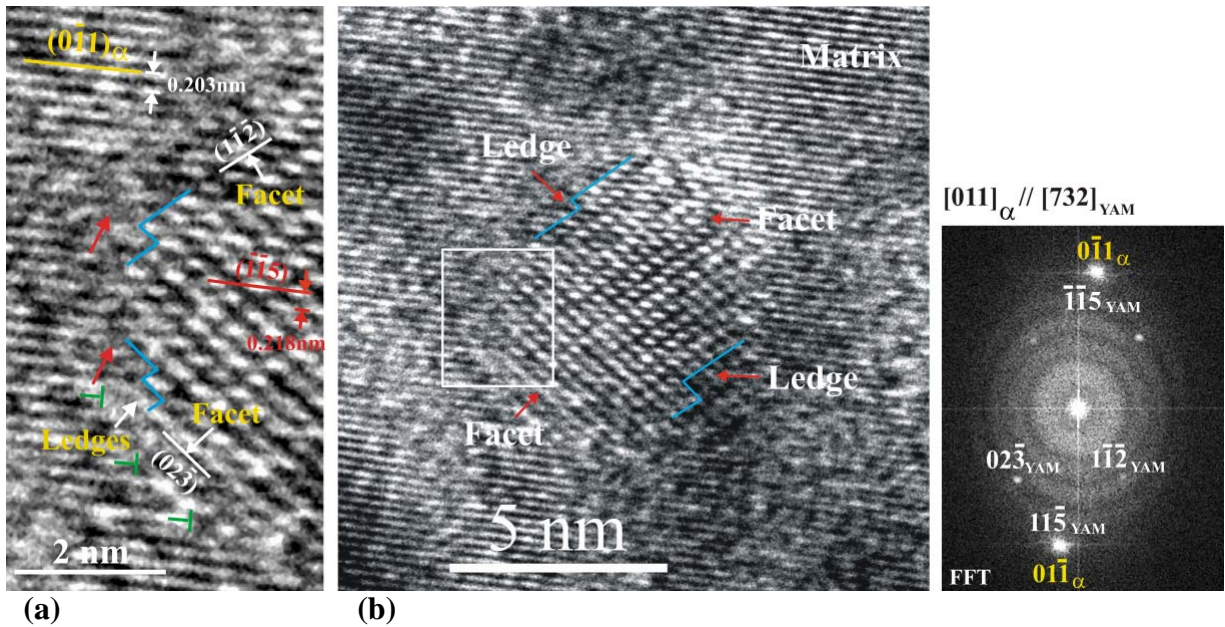Fig. 3. HRTEM images of a large $Y_4Al_2O_9$ (YAM) nanoparticle at two different defocus conditions (a) -75 nm, (b) -50 nm.

Fig. 4. HRTEM images of a small $Y_4Al_2O_9$ (YAM) nanoparticles; (a) The oxide/matrix interfacial structure observed from the marked area shown in (b). Facets, ledges, dislocations, and thin layer of featureless domains (marked by red arrows) can be readily seen at the interfaces. The orientation relationship between the nanoparticle and the matrix can be derived from the FFT image.
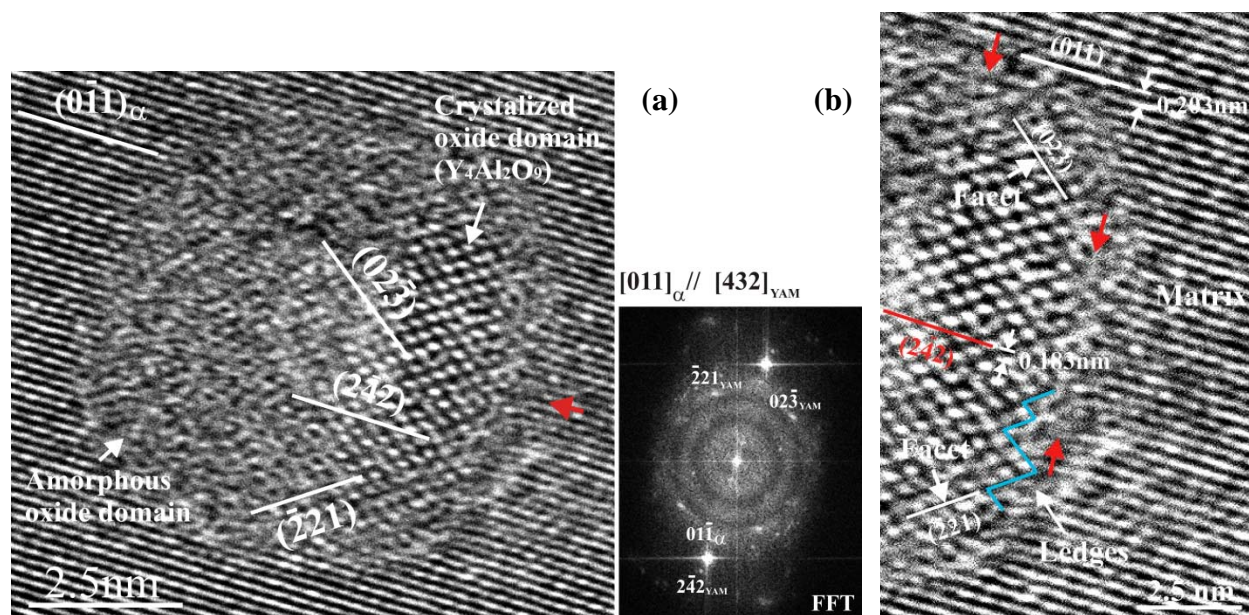
Fig. 5. HRTEM images show (a) the nucleation of a crystalline $Y_4Al_2O_9$ domain (2 x 5 nm) in an amorphous oxide particle; (b) facets, ledges, and amorphous remnant (marked by red arrows) can be seen at the oxide/matrix interface (indicated by a red arrow in (a)). Orientation relationship between the $Y_4Al_2O_9$ crystalline domain and the matrix can be derived from the FFT image.
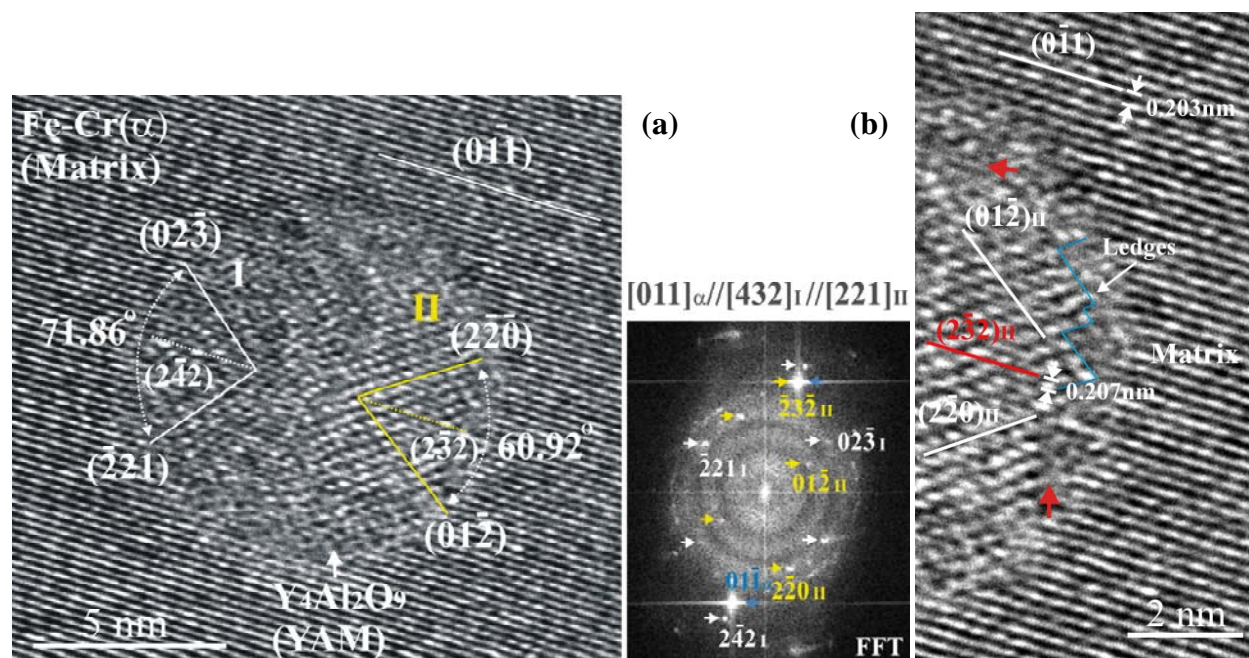

Fig. 6. HRTEM images show (a) the formation of multiple $Y_4Al_2O_9$ domains within an oxide nanoparticle and (b) facets, ledges, and amorphous remnant (marked by red arrows) can be found at the interface between the oxide (domain II) and the matrix.
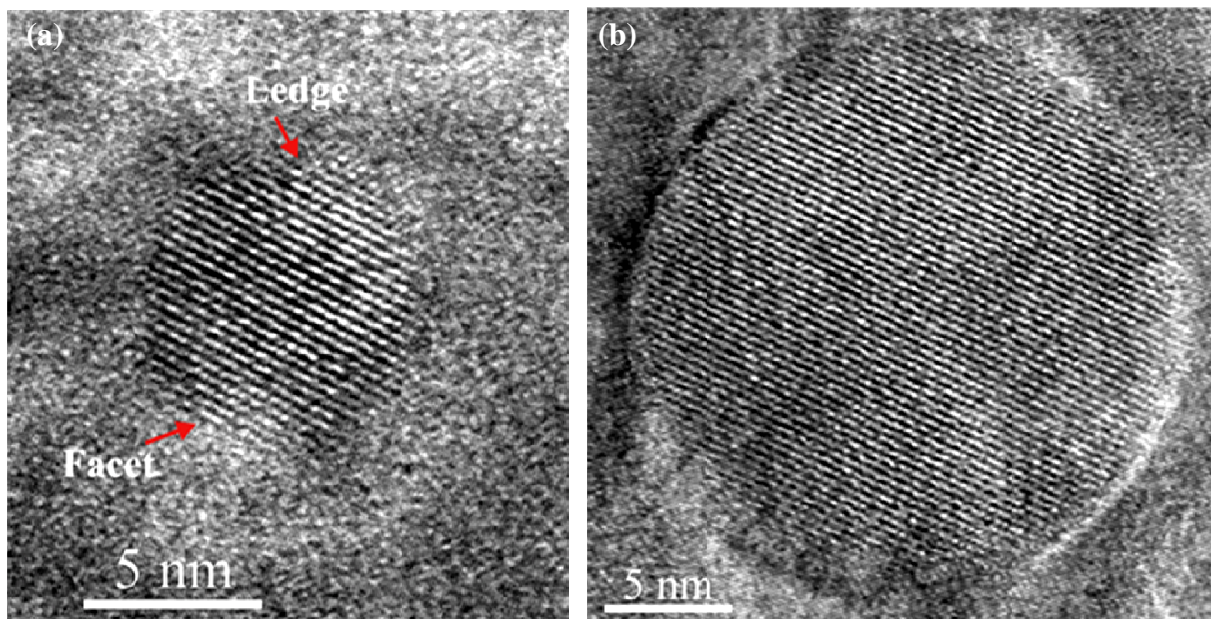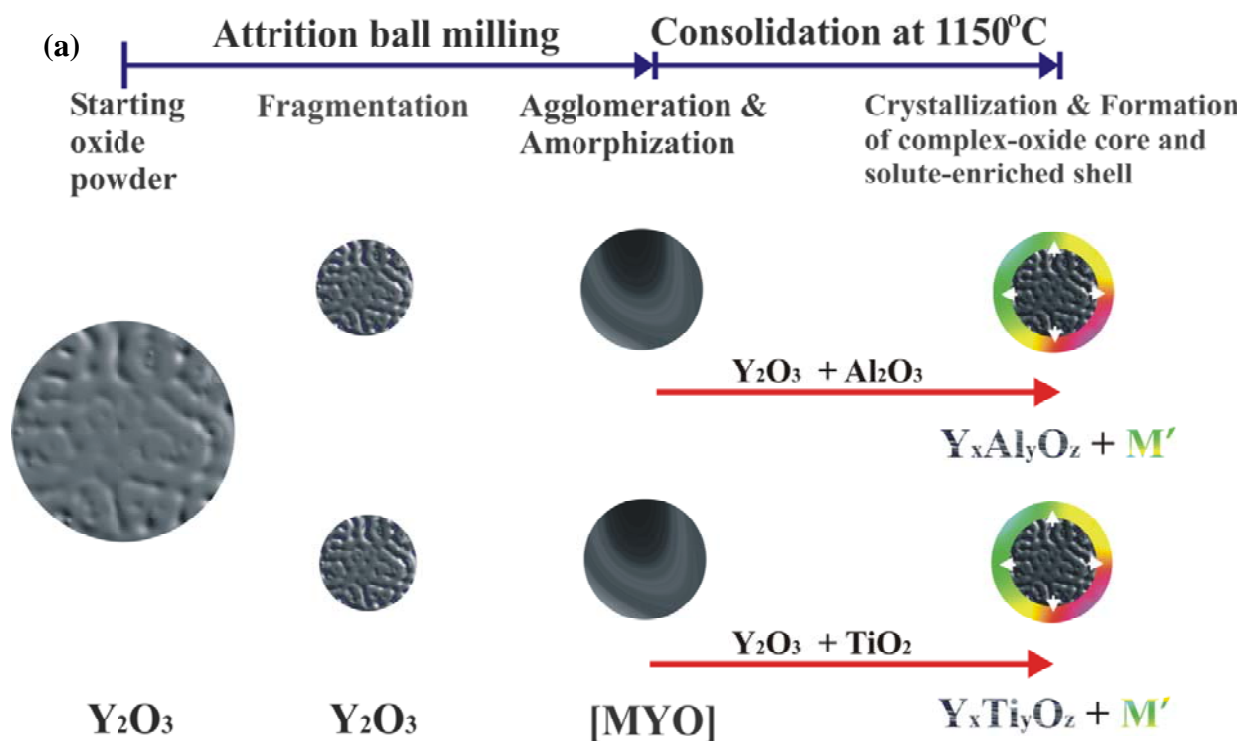
Fig. 7. HRTEM images of (a) a small nanoparticle (d < 10 nm) and (b) a large nanoparticle (d > 20 nm) and after prolonged annealing at 900 °C for 168 hours. Notice that the small nanoparticle remains faceted and the large nanoparticle becomes perfectly spherical and fully crystallized without a core/shell structure.
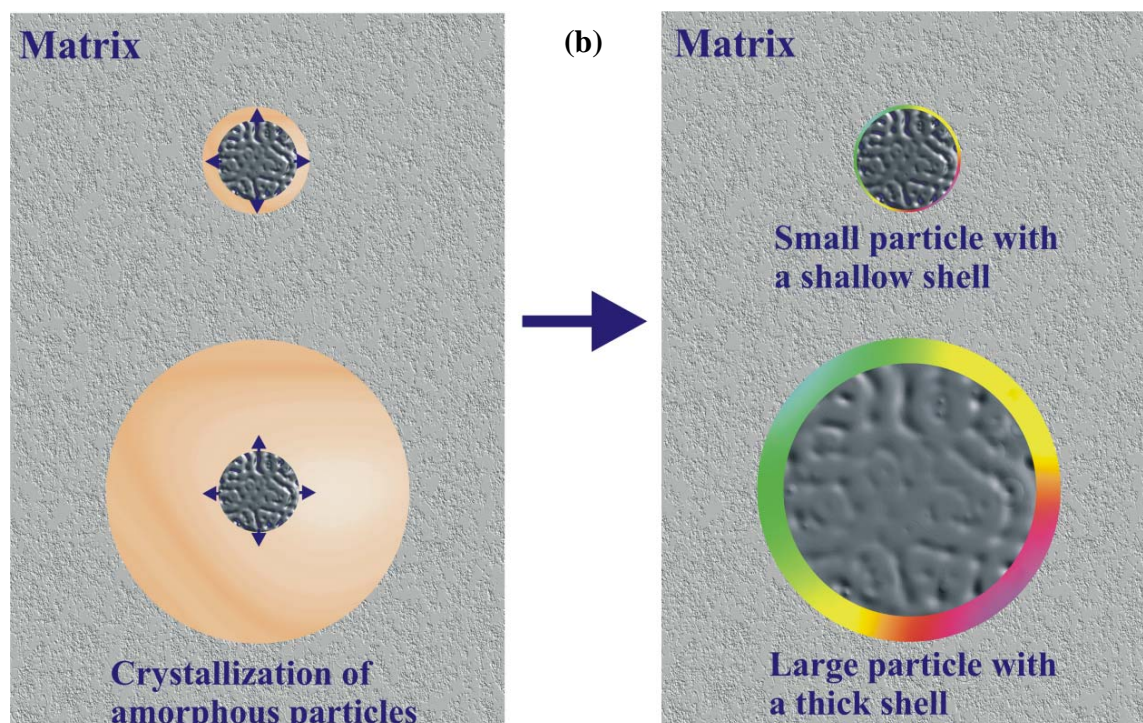
Fig. 8. Schematic illustrations show (a) a three-stage mechanism for the formation of oxide nanoparticles containing a core/shell structure during a mechanical alloying process and (b) size effect on the formation of core/shell structures in oxide nanoparticles; a solute-enriched shell forms when solute depletion rate from the core is greater than solute diffusion rate from the oxide/matrix interface during the crystallization stage.

References

[1] Ehrlich K, Phil. Trans. R. Soc. Lond. A 357, 1999: 595-623.

[2] Ukai S, Fujiwara M, J. Nucl. Mater. 307-311, 2002: 749-757.

[3] Kasada R, Toda N, Yutani K, Cho HS, Kishimoto H, Kimura A, J. Nucl. Mater. 367-370, 2007: 222-228.

[4] Okuda T, Fujiwara M, J. Mater. Sci. Lett. 14, 1995: 1600-1603.

[5] Kimura Y, Takaki S, Suejima S, Uemori R, Tamehiro H, ISIJ International, 39 (2), 1999: 176-182.

[6] Sakasegawa H, Tamura M, Ohtsuka S, Ukai S, Tanigawa H, Kohyama A, Fujiwara M, J. Alloys & Compounds 452, 2008: 2-6.

[7] Alinger MJ, Odette GR, Hoelzer DT, Acta Mater. 57, 2009: 392-406.

[8] Marquis EA, Appl. Phys. Lett. 93, 2008: 181904.

[9] Klimiankou M, Lindau R, Möslang A, J. Nucl. Mater. 386-388, 2009: 553-556.

[10] Yutani K, Kishimoto H, Kasada R, Kimura A, J. Nucl. Mater. 367-370, 2007: 423-427.

[11] Uki S, Nishida T, Okada H, Okuda T, Fujiwara M, Asabe K, J. Nucl. Sci. Technol. 34 (3), 1997: 256-263.

[12] Christensen AN and Hazell RG, Acta Chemica Scandinavica 45, 1991: 226-230.

[13] Ching WY, Xu YN, Physical Review B 59 (20), 1999: 12815-12821.

[14] de Castro V, Leguey T, Monge MA, Munoz A, Pareja R, Amador DR, Torralba JM, Victoria M, J. Nucl. Mater. 322, 2003: 228-234.